Non-syndromic Mitral Valve Dysplasia Mutation Changes the Force Resilience and Interaction of Human Filamin A

Tatu J.K. Haataja, Rafael C. Bernardi, Simon Lecointe, Romain Capoulade, Jean Merot, and Ulla Pentikäinen Jean Merot,

- 1. Department of Biological and Environmental Science and Nanoscience Center, University of Jyväskylä, 40014 Jyväskylä, Finland
- 2. Beckman Institute for Advanced Science and Technology, University of Illinois at Urbana-Champaign, Urbana, IL 61801, USA
- 3. Institute of Biomedicine, University of Turku, 20520 Turku, Finland
- 4. Turku Centre for Biotechnology, University of Turku, 20520 Turku, Finland
- 5. L'institut du Thorax, INSERM, CNRS, UNIV Nantes, Nantes, France
- *Corresponding author: ulla.pentikainen@utu.fi

Abstract

Filamin A (FLNa), expressed in endocardial endothelia during fetal valve morphogenesis, is key in cardiac development. Missense mutations in FLNa cause non-syndromic mitral valve dysplasia (FLNAMVD). Here, we aimed to reveal the currently unknown underlying molecular mechanism behind FLNA-MVD caused by the FLNa P637Q mutation. The solved crystal structure of the FLNa3-5 P637Q revealed that this mutation causes only minor structural changes close to mutation site. These changes were observed to significantly affect FLNa's ability to transmit cellular force and to interact with its binding partner. The performed steered molecular dynamics simulations showed that significantly lower forces are needed to split domains 4 and 5 in FLNA-MVD than with wild-type FLNa. The P637Q mutation was also observed to interfere with FLNa's interactions with the protein tyrosine phosphatase PTPN12. Our results provide a crucial step toward understanding the molecular bases behind FLNA-MVD, which is critical for the development of drug-based therapeutics.

Introduction

Mitral valve diseases are a heterogeneous group of phenotypically distinct valvular disorders characterized by malformations in heart valves. Valvular diseases affect approximately 3% of the population and remain one of the most common indications for valvular surgery (Levine et al., 2015). Familial inheritance of valvular disorders has been largely recognized after the first missense mutations associated with inherited mitral valve dysplasia (MVD) were identified in the X-chromosomal human gene Filamin A (FLNA) (FLNA-MVD; OMIM 314400) (Levine et al., 2015; Kyndt et al., 2007). The four missense mutations G288R, P637Q, V711D, and H743P (Figure 1A) identified in FLNA-MVD patients determined thickened myxomatous "Barlow-like" leaflet dystrophy (Bernstein et al., 2011; Kyndt et al., 2007; Le Tourneau et al., 2017). Our recent and comprehensive echocardiographic evaluation of >150 FLNA-MVD patients further unveiled the unique and homogeneous phenotype of FLNA-mitral valve prolapse (MVP). It is characterized by peculiar mitral valve features, such as an unusual combination of leaflet prolapse in systole associated with restrictive motion in diastole, and a heterogeneity in the remodeling of the valve (i.e., different at the free edge versus the body or annulus area of the leaflet). Moreover, the mitral valve apparatus presents distinctive characteristics: the chordae are shorter and the

papillary muscles are displaced close to the annulus. Importantly, FLNA-MVD patients also present polyvalvular disorders, especially affecting the aortic valve (Le Tourneau et al., 2017). Interestingly, both developmental and degenerative processes have been reported: echography of an affected pregnant woman has revealed the presence of a dystrophic mitral valve for the fetus and, at the same time, analysis of the time course of the disease in a large cohort of FLNA-MVD patients demonstrated a continuous degenerative process leading to the thickening and remodeling of the valve with aging.

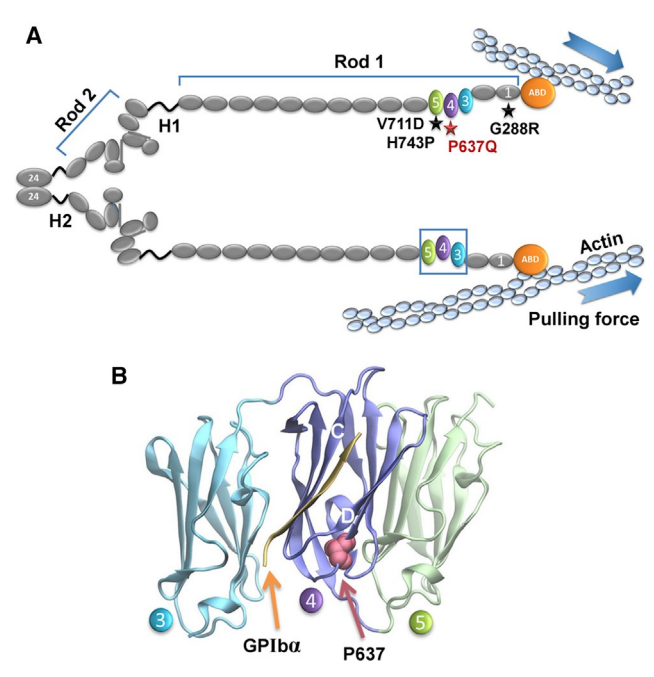


Figure 1. Schematic Representation of Filamin. Schematic representation of FLNa dimer having 24 lg domains (gray) and the actin-binding domain (ABD, orange) in a monomer. The two monomers are dimerized via domain 24, which is separated from rod 2 via flexible hinge 2 (H2). Hinge 1 (H1) connects rod 1 to rod 2. The three domain 3–5 fragment studied here is colored in blue, purple, and green. The localizations of FLNAMVD mutations have been highlighted with stars. Actin with the direction of pulling force is shown in light blue. The crystal structure of FLNa3-5 WT (PDB: 4M9P) and the binding mode of GPlba peptide to FLNa domain 4. The FLNa3-5 peptide structure is obtained by superimposing FLNc4-5 X-ray structure (PDB: 4MGX) with FLNa3-5 structure. The peptide has been colored in orange. P637, whose mutation to glutamine residue cause FLNA-MVD, is highlighted with space filling model.

Key for cardiac development, Filamin A (FLNa, Figure 1A) is a ubiquitously expressed actin-crosslinking protein (van der Flier and Sonnenberg, 2001). In particular, FLNa is expressed in endocardial endothelia during fetal valve morphogenesis. FLNa knockout leads to embryonic lethality with a pleomorphic array of cardiac malformations (Feng et al., 2006; Stossel et al., 2001). At the molecular level, FLNa provides a link between the cytoskeleton and the cell surface, and FLNa has been identified to be a central element in cellular mechanotransduction (Ehrlicher et al., 2011; Zhou et al., 2010). Endocardial cell mechanotransduction has been shown to play a critical role in all aspects of heart development, including valve development (McCormick and Tzima, 2016), and defective response to forces is known to underlie many medical conditions, such as cardiac diseases (Herum et al., 2017; Levine et al., 2015; Lyon et al., 2015). FLNa also plays an important role in cellular signal transmission, with more than 90 identified binding partners that include transmembrane receptors and signaling molecules (Zhou et al., 2010).

Therefore, FLNa has essential scaffolding functions and integrates multiple cellular behaviors during embryonic development, cellular migration, and mechanical stress responses (Baldassarre et al., 2009; Norris et al., 2010; Zhou et al., 2010). Structurally, FLNa is a homodimer, composed of N-terminal actin-binding domains followed by 24 homologous immunoglobulin (Ig)-like domains of which domains 3–5 and 16–21 form tightly arranged compact substructures in otherwise flexible Ig-domain rods (Figure 1) (Ruskamo et al., 2012; Sethi and Ylänne, 2014; Sethi et al., 2014).

The underlying mechanisms behind valvular diseases are, in general, poorly understood. Here, we provide the first comprehensive study that aims to elucidate molecular level changes in FLNA-MVD caused by the P637Q mutation, the most common mutation found in FLNA-MVD patients. The P637Q mutation is located at FLNa domain 4 (FLNa4), which is the central domain within the tightly arranged three domain FLNa3-5 fragment (Sethi et al., 2014) (Figure 1). This study was aimed to investigate how the P637Q mutation that causes FLNA-MVD (1) changes the structure of FLNa, (2) affects FLNa's ability to transmit cellular forces, and (3) affects FLNa's interactions with other proteins.

Results

The P637Q Mutation Has a Minor Effect on FLNa3-5 Wild-type Structure

In order to get information how MVP-causing mutation P637Q affects FLN's structure, the P637Q mutation was inserted in the three-domain fragment consisting of domains from 3 to 5. As we earlier solved the wild-type (WT) structure of the FLNa3-5 fragment (Sethi et al., 2014), the newly introduced mutant into this same construct enabled reliable comparison of WT and mutant structures. Both X-ray crystallography and small angle X-ray scattering (SAXS) were employed in the structure characterization. The FLNa3-5 P637Q fragment produced fragile, large, rugged, rod-like crystals that were 2 mm in the longest edge. The diffraction data were collected and the obtained crystals belonged to space group P65 and diffraction data up to 2.1 Å were used (Table 1). The structure was solved by molecular replacement using the WT structure (PDB: 4M9P) as a search model. The electron densities of Gly764—Gly766 were not seen, and therefore they were excluded from the final model. The structure of FLNa3-5 P637Q mutant was deposited to PDB with accession code 6EW1.

The obtained crystal structure of FLNa3-5 P637Q mutant revealed that the overall fold of WT FLNa is not affected by the P637Q mutation (Figures 2A and 2B). Only the loop between E and F strands is slightly shifted toward neighboring B strand in the mutant structure where the proline residue is replaced with the glutamine residue (Figure 2B). The calculated root mean square deviation between the mutant and the WT (Sethi et al., 2014) structure is 0.84 Å (286 Ca atoms). Interestingly, although the overall WT and mutant structures are highly similar, the local interactions at the mutation site are affected due to the mutation of a hydrophobic proline to a polar glutamine residue. In the WT structure, only the P637 main-chain carbonyl group is hydrogen bonded to the main-chain amide group of G592 (Figure 2C). This hydrogen bond is also present in the mutant structure, but the strength is increased due to the shift of the E-F loop (Figure 2D). In addition, there are two new hydrogen bonds formed in the mutant structure: one between the side-chain amide group of Q637 and the main-chain carbonyl group of K593, and the other one between the side-chain carbonyl group of Q637 and the main-chain amide of E639 (Figure 2D). However, the P637Q mutation not only introduces new stabilizing interactions but the favorable contact

seen between the I663 side chain and P637 is transformed to an unfavorable one in the mutant structure (Figures 2C and 2D). The closer inspection of protein structures also revealed that P637Q mutation causes changes on the hydrogen bonding network at the protein surface (Figure 3). In the WT structure, a hydrogen bonding network is seen between W636, E622, and R634 (Figure 3A). This network is absent in P637Q mutant structure where W636 forms a hydrogen bond with G592 (Figure 3B). The changes in the hydrogen bonding pattern are due to the restricted main-chain angles of proline being substituted with the more flexible main chain of glutamine. However, due to the mutation, the main chain is straightened, and therefore W636 favors conformation where the hydrogen bond is formed with G692 (Figures 3B versus 3A). Due to these changes in the hydrogen bond network, and especially orientation of the W636 side chain, the shape and electrostatic potential surface properties differentiate at a relatively large surface area (Figures 3C and 3D).

Table 1. Data Collection and Refinement Statistics for FLNa3-5 P637Q Crystals Structure

^bValues in parentheses are for highest-resolution shell.

	FLNa3-5 P637Q ^a	
Data Collection		
Wavelength (Å)	0.961	
Resolution range	37.81–2.31	(2.389-2.307) ^b
Space group	P6 ₅	
Mosaicity (degrees)	0.1	
Unit cell dimensions		
a, b, c (Å)	60.72, 60.72, 163.18	
α, β, γ (°)	90, 90, 120	
Total reflections	177,320	(17,776)
Unique reflections	14,953	(1482)
Completeness	1.0	(0.99)
CC _{1/2}	1.0	(0.97)
Ι/σΙ	36.96	(7.1)
R _{meas}	0.00396	(0.331)
Multiplicity	11.9	(12.0)
Refinement		
No. reflections	14,951/1,483	
R _{work} /R ^{free}	0.245/0.274	
No. of atoms		
Macromolecule	2,165	
Solvent	53	
B-factors (A ²)		
Macromolecule	71.6	
Solvent	53.0	
Root-mean-square deviations		
Bonds (Å)	0.003	
Angles (°)	0.65	
Ramachandran statistics (%)		
Favored	95.0	
Allowed	4.5	
Outliers	0.0	
Rotamer outliers (%)	3.9	

^aDiffraction data from a single crystal were used.

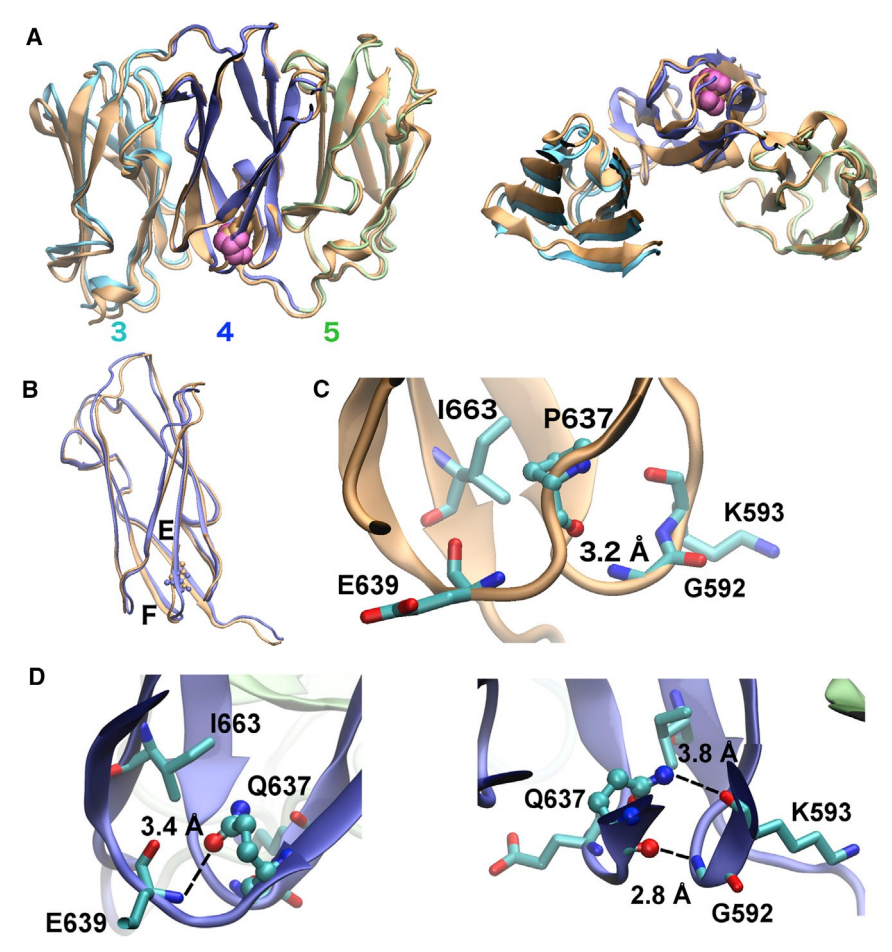


Figure 2. FLNA-MVD Causing P637Q Mutation Changes the Interactions at the Mutation Site. The superposition of FLNa3-5 WT (PDB: 4M9P, shown in gold) and the P637Q mutant structures show that the P637Q mutation does not affect the overall FLNa structure. Both P637 and Q637 are shown as space-filling models. The superposition of the WT and P637Q structures are shown in two different orientations. The replacement of P637Q with Q637 slightly shifts the loop between strands E and F toward A-B loop. Only domains 4 from both FLNa3-5 WT (gold) and FLNa3-5 P637Q (blue) structures are shown. Q637 and P637 are shown as ball and stick. Only one hydrogen bond is formed at the mutation site of WT FLNa3-5, between main-chain amide group of G592 and main-chain carbonyl group of P637Q. The hydrophobic contact between I663 and P637 also stabilizes the mutation site. New hydrogen bonds between Q637 side chain and E639 main chain, and Q637 side chain and K593 main chain are formed due to P637Q mutation. In addition, the hydrogen bond between mainchain amide group of G592 and main-chain carbonyl group of Q637 is strengthened compared with WT due to the shift of the E-F loop toward the A-B loop.

To exclude the possibility of crystallographic artifacts, the structural properties of the FLNa3-5 WT and P637Q mutant fragments were also investigated in solution using SAXS. Scattering profiles obtained from SAXS measurements from the WT and mutated FLNa3-5 fragments are identical, indicating that both protein fragments have a similar shape (Figure 4A). Also, the particle dimensions calculated from scattering data are identical (Table 2). The theoretical scattering curve calculated from the crystal structure of FLNa3-5 P637Q fits well to the experimentally determined one (c = 1.1), further supporting that the solid-state crystal structure well represents the structure that protein adopts in solution (Figure 4C). For comparison, the c value of 1.0 was obtained for WT protein (Figure 4B). The generated ab initio

envelopes of the WT and mutant FLNa3-5 fragments are highly similar and fit the corresponding crystal structures well (Figures 4B and 4C). Taken together, the solved FLNa3-5 P637Q crystal structure represents the structure that this protein fragment adopts in solution.

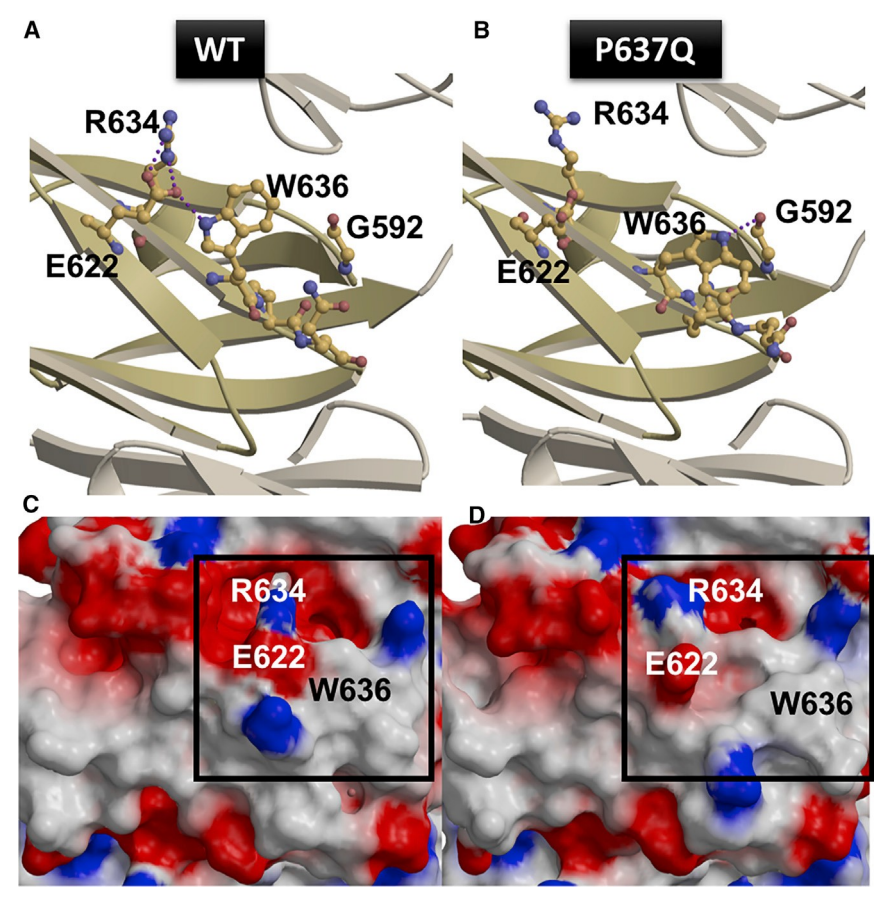


Figure 3. FLNA-MVD Causing P637Q Mutation Changes the Shape and Electrostatic Potential of the Mutation Site. (A and B) The hydrogen bonding network at the surface of FLNa4 is different; in WT (A), W636 is hydrogen bonded with R634, whereas, in the P637Q structure (B), the orientation of W636 is changed and the hydrogen bond with R634, seen in the WT structure, is no longer possible but W636 forms a new hydrogen bond with G592. (C and D) The changes in the W636 orientation in WT (C) and P637Q (D) structures affect the shapes and electrostatic potential of the surfaces of the domain; in the P637Q (D), the surface is flatter and more hydrophobic than in WT (C).

In order to evaluate whether the P637Q mutation induces flexibility to FLNa3-5 in terms of particle dimensions, ensemble optimization method (EOM) analyses were performed on the SAXS data. The obtained distributions for the generated pools of random models and the selected models were highly similar between the WT and mutated fragments, indicating that the P637Q mutation does not increase the flexibility of the FLNa4-FLNa5 interaction (Figure S1). The structures obtained from EOM calculations fit well onto the experimental scattering data in both examined fragments (Figure S1). The average maximum dimension (Dmax) of the selected pool was 7.3 nm for both the WT and P637Q mutant, while the average radius of gyration (Rg) was 2.2 nm for the WT and 2.3 nm for the mutant.

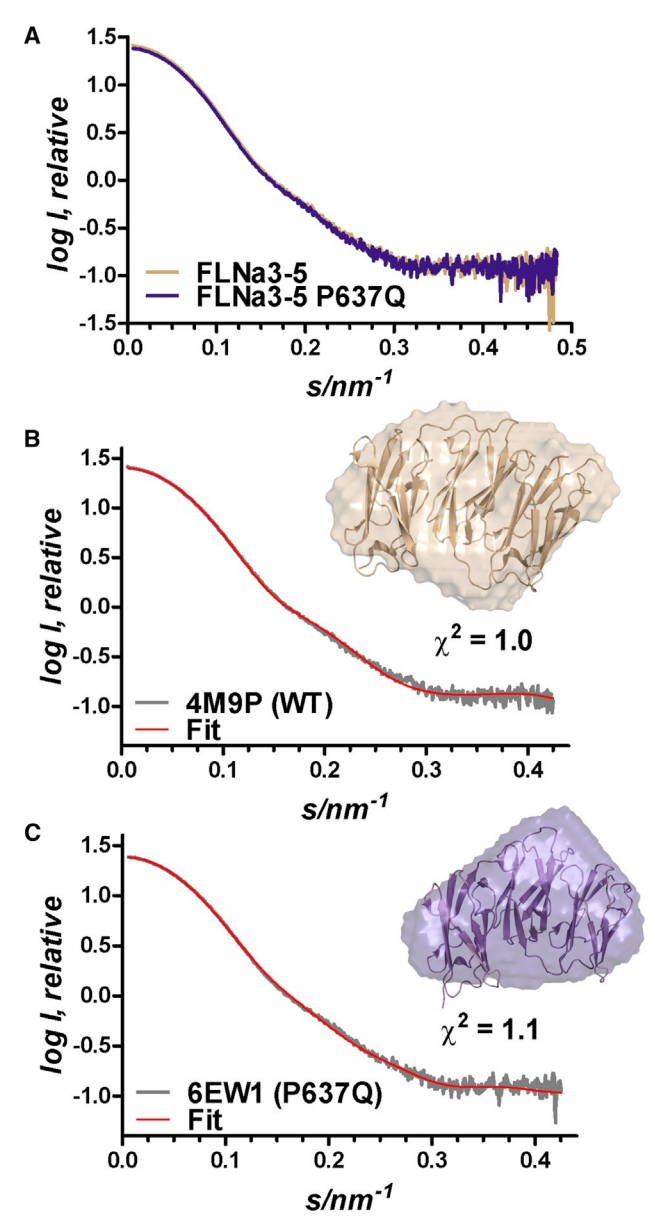


Figure 4. Both WT and P637Q FLNa Have Similar Structures in Solution. Superposition of experimental scattering curves obtained from SAXS measurements of FLNa3-5 WT and P637Q shows that the shapes of both protein fragments are identical. The theoretical scattering curve of FLNa3-5 (4M9P) calculated from the crystal structures and the fit against the experimental scattering data shows that the crystal structure also resembles the structure in solution. The superposition of the crystal structure of WT with the averaged SAXS envelope further confirms similarity of the solution and X-ray structure. The normalized spatial discrepancy (NSD) of superposition is 1.38. Similarly, as for WT (B), the theoretical scattering curve of FLNa3-5 P637Q (6EW1) calculated from the crystal structures and the fit against the experimental scattering data shows that the crystal structure also resembles the structure in solution. The superposition of the crystal structure of FLNa3-5 P637Q with the averaged SAXS envelope further confirms similarity of the solution and X-ray structure. The NSD of superposition is 1.49.

The influence of the P637Q mutation on the stability of the tight FLNa4-FLNa5 interaction compared with the WT structure (Sethi et al., 2014) was further investigated using molecular dynamics (MD) simulations. Previously, three amino acids at the FLNc4FLNc5 interface, W577, D627, and R755, had

been identified as crucial for the stability of the tight domain-domain interaction (Sethi et al., 2014). MD simulations (100 ns) were performed in triplicates for both FLNa4-5 WT and P637Q fragments using the known atomic detailed X-ray structures as starting points. The stability of the FLNa4-FLNa5 interaction was then analyzed from the MD trajectory obtained. The interaction distances between the amino acids at the domain-domain interface were calculated and interactions were observed to remain stable during the entire simulation (Figure S2). Similar results were obtained from all three independent simulations. In summary, the P637Q mutation affects only the structure and interaction close to the mutation site but not the overall fold or flexibility of FLNa3-5.

Table 2. The Molecular Dimensions of FLNa3-5 WT and P637Q Calculated from SAXS Data. The values marked with asterisks are calculated for the merged scattering of high and low concentration data.

a. Radius of gyration (Rg); estimated error is ±0.1 nm.

Sample	c (mg/mL)	Rg (nm) ^a	<i>Dmax</i> (nm) ^b
FLNa3-5	1.0	2.2	7.2
	2.0	2.2	7.2
	4.0	2.2	7.3
		2.2*	7.2*
FLNa3-5 P637Q	1.0	2.2	7.4
	2.0	2.2	7.4
	4.0	2.2	7.4
		2.2*	7.4*

The Effect of FLNA-MVD Mutation on FLN's Force Resilience

Shear stress and mechanotransduction are crucial for valve development (Butcher and Nerem, 2007; McCormick and Tzima, 2016) and defective force responses underlie many cardiac medical conditions (Herum et al., 2017; Krüger and Linke, 2009; Lyon et al., 2015). FLNa has been identified as one of the key mechanotransduction elements of the cytoskeleton (Ehrlicher et al., 2011). So far, only the role of rod 2 domains in FLN mediated mechanotransduction has been studied (Pentikäinen and Ylänne, 2009; Rognoni et al., 2012; Seppälä et al., 2017), whereas rod 1 domain behavior under force has remained enigmatic. Therefore, we first employed steered MD (SMD) simulations to investigate how mechanical stress changes the compact structure of WT FLNa4-5 (Figure 5A). The obtained results revealed that the domain-domain interaction opens before the unfolding of domains 4 and 5 (Figure 5A). The SMD simulations were repeated in an enhanced sampling approach 50 times and, in all cases, the opening of the domain-domain interface occurred first. However, three post-detachment scenarios emerged: either domain 4 or domain 5 was the first to unfold, or simultaneous unfolding of both domains was observed. Accordingly, based on SMD simulations, the FLNa4-5 fragment is regulated by the force. In order to evaluate the effects of FLNA-MVD causing the P637Q mutation on FLNa's force resilience, similar SMD simulations were performed for the FLNa4-5 P637Q fragment using the X-ray structure reported here as a starting point. The SMD simulations were repeated 30 times and the mutant's behavior matched to WT. In all simulations, the domain-domain interface opened first, followed by unfolding of both domains simultaneously or subsequently (Figure 5A). Importantly, although the unfolding profiles for FLNa4-5 WT and mutated fragments were similar, the forces needed to break the domain-domain interaction were

strikingly different. The maximum forces needed to unfold the domaindomain interface were calculated from trajectories (N = 50 for WT, N = 30 for the mutant) obtained from SMD simulations. Interestingly, for P637Q mutated FLNa4-5, the average of maximum forces needed to open the domain-domain interface is significantly lower than for WT, as seen from the histograms shown in Figure 5B. The average force needed for domain-domain opening was 786 pN for WT (N = 50) and 668 pN for P637Q mutant (N = 30).

How mechanical signals are transmitted through FLNa4-5 was analyzed employing a crosscorrelation-based network analysis. The force propagation pathways were calculated for all SMD trajectories obtained for both WT and P637Q mutants. The calculated pathways for WT and P637Q mutants were different, as can be seen in Figures 5C and 5D, respectively. With FLNa4-5 WT, only one pathway, which directly connects FLNa4 and FLNa5, was observed (Figure 5C). For the FLNa4-5 P637Q mutant, two distinct pathways were seen, one similar to WT, and another that goes via K593. In the crystal structure of FLNa3-5 P637Q, the amide group of Q637 forms a hydrogen bond with the main-chain carbonyl group of K593. This interaction is not possible with FLNa3-5 WT, which has a hydrophobic proline residue at position 637. In addition, we investigated the communities formed in the systems by employing dynamic network analysis and generalized correlation. These communities, shown in Figures 5E and 5F, correspond to sets of residues that move in concert with each other and can be used to investigate regions that are generally more strongly connected during pulling simulations. Community analysis revealed that little inter-domain correlation is found in both WT and P637Q mutants. The same analysis also revealed that P637 (WT) and Q637 (mutant) are central amino acids in a highly correlated community, which indicates that the P637Q mutation could cause disturbance in the dynamics of the complex. Accordingly, the altered local interactions between WT and P637Q mutant at the mutation site seem to be the reason for the different force resilience between WT and P637Q FLNa4-5.

The Effects of FLNA-MVD Mutation on FLNa's Interactions

FLNa executes many of its functions via interactions with other proteins (Nakamura et al., 2007; Razinia et al., 2012; Zhou et al., 2010). Accordingly, the obvious mechanism for FLNAMVD caused by the P637Q mutation would be the altered interactions with other proteins, followed by the effects on downstream signaling. The GPIba adhesion receptor binds in a groove between the b strands C and D (CD face) of domain 4 by forming an additional b strand (Sethi et al., 2014) (Figure 1B) and is a prototype of many FLNa interacting proteins (Ithychanda et al., 2009). The X-ray structure of FLNa3-5 P637Q, presented here, reveals that the P637Q mutation does not alter the CD-face structure compared with that seen in the WT fragment. We tested the binding affinity in solution in order to exclude the possibility of the solid-state artifacts. The affinity of GPIba peptide for the purified FLNa4 WT and P637Q was determined using pull-down experiments. As expected, the results show that the affinity of GPIb peptide is similar to both WT and mutant (Figure 6A).

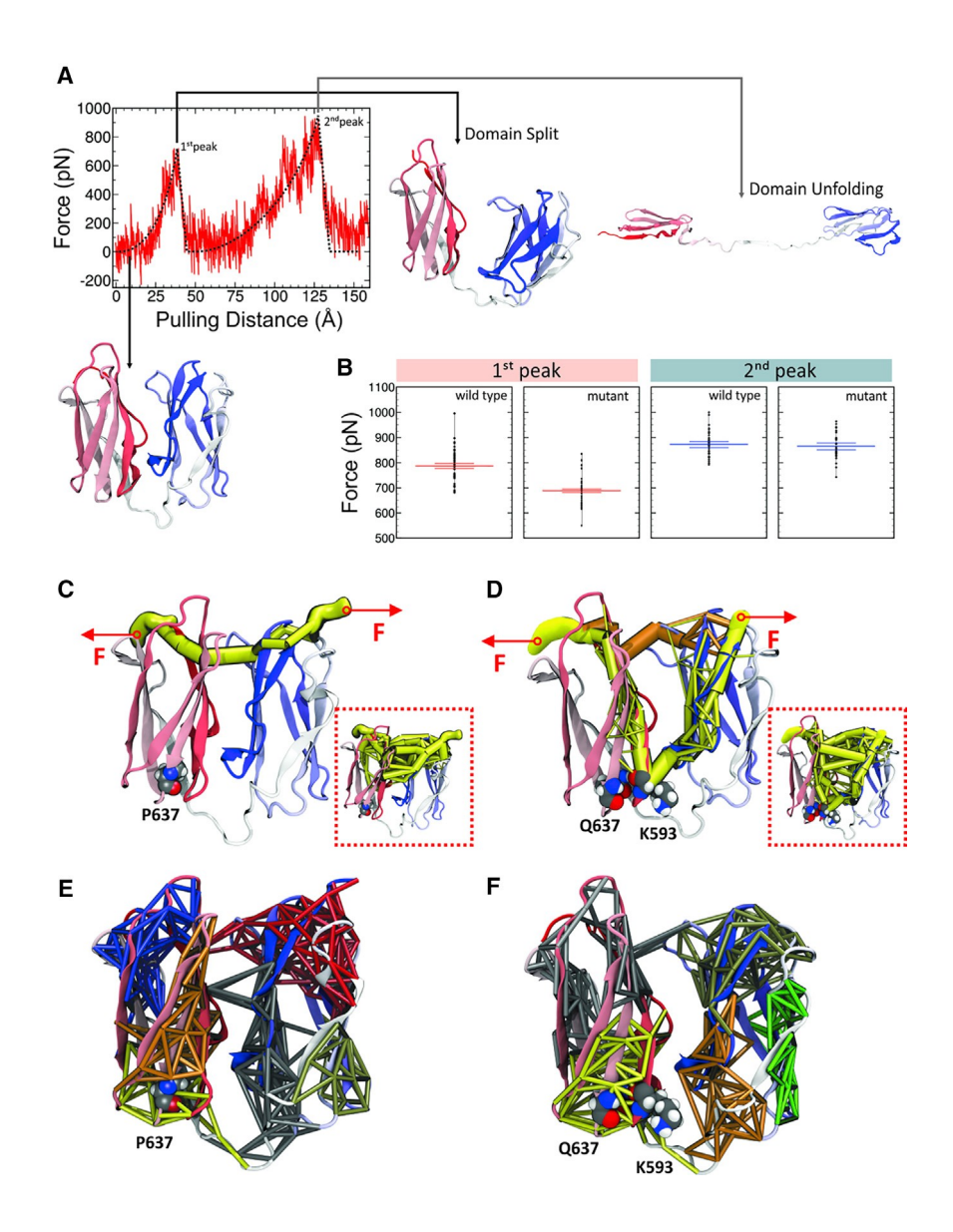


Figure 5. Mechanostability and Force Propagation Pathways Are Changed in FLNAMVD. An example force versus distance profile obtained using SMD. The first peak corresponds to the split between FLNa domains 4 and 5. Second peak corresponds to domain unfolding. SMD peak splitting (first peak) and unfolding (second peak) forces from each simulation replica (black dots) and average peak force (red or blue lines) ± SEM. Forces to split domains FLNa4 from FLNa5 are much lower for mutant than for WT; however, no significant difference is observed in the unfolding forces. (C and D) Force propagation pathways through WT and P637Q (D) FLNa4-5 calculated using Pearson correlation (yellow tubes). The thickness of the pathway edges represents the normalized probability of force propagating through the particular edge. For the mutant, two distinct force propagation pathways were observed (D), one directly connecting FLNa4 to FLNa5 (orange tubes), in a similar way to the pathway observed for the WT construct; another (yellow tubes) shows a much longer pathway, indicating a smaller correlation between domains 4 and 5. (E and F) Network-based community analysis in WT (E) and P637Q (F) FLNa4-5 showing regions with high internal correlation during pulling simulations calculated using generalized correlation. Communities are colored individually, showing little interdomain correlation. It is clear in both (E) and (F) that the mutation region is central for one of the highly correlated communities.

PTPN12 has been reported to interact with rod 1 domains 1–8 (Duval et al., 2015). As the exact PTPN12 binding domain(s) and binding mode on FLNa were not known, we first tested to which FLNa domains PTPN12 binds. The pull-down binding assays were performed using the purified single FLNa domains FLNa1, FLNa3, FLNa4, FLNa5, and FLNa6 and the PTPN12 proline-rich Pro4 domain (672DSPPPLPERTPES684), previously identified as the FLNa-PTN12 interaction domain (Duval et al., 2015; Playford et al., 2006). The results clearly show that FLNa4 is the main binding site but domains 3, 5, and 6 also show some binding affinity to PTPN12, whereas FLNa1 does not (Figure 6B). We further tested the interaction of longer PTPN12 fragments with FLNa4-6 WT and P637Q using surface plasmon resonance (SPR). As illustrated in Figure 7A, the C-terminal domain of PTPN12 (PTPN12-600-780) containing Pro4 domain interacted with WT FLNa4-6 (Kd z 330 nM). Shorter PTPN12-600-709 and 634–709 peptides also containing the Pro4 domain also interacted with FLNa4-6 with similar Kd values (320 and 270 nM, respectively). On the other hand, the PTPN12-600-634 and 600–673 fragments missing the Pro4 domain did not interact with FLNa4-6 (Kd > 10 mM). Interestingly, when C-terminal PTPN12 domain (600–780) binding to mutant FLNa4-6 P637Q was tested, no interaction was detected (Figure 7B), although the Pro4 domain alone binds similarly to both WT and P637Q FLNa4 (Figure 6B).

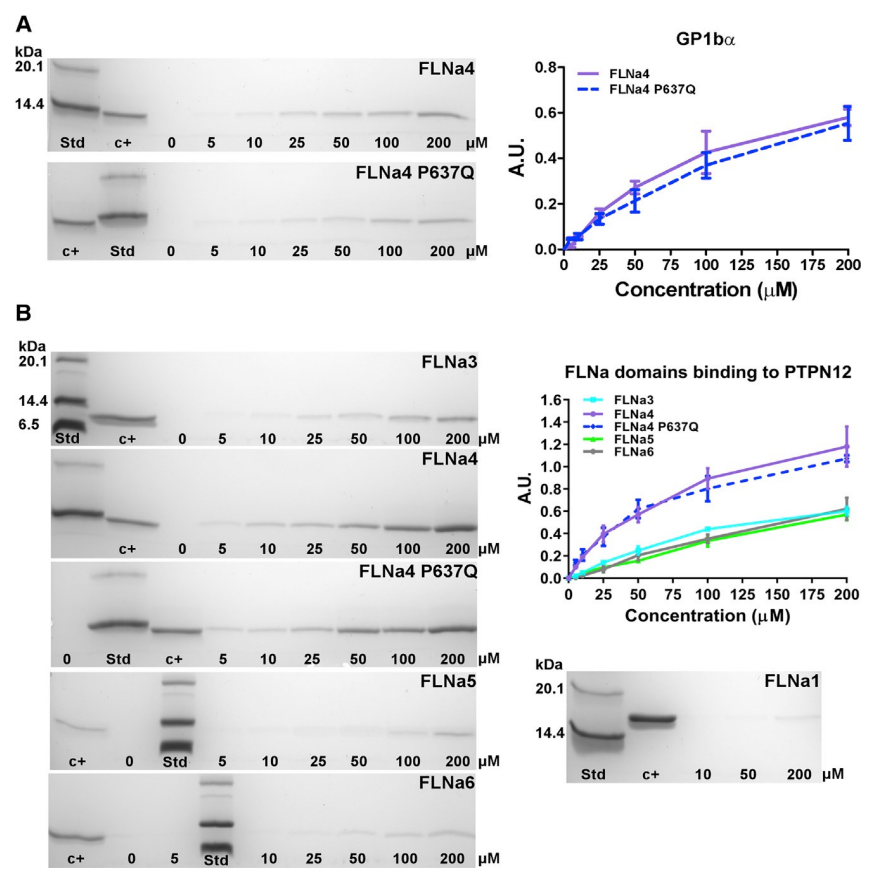


Figure 6. The P637Q Mutation Does Not Influence the GPIba peptide or PTPN12 Pro4 Domain Binding to FLNa. GPIba peptide binding to FLNa4 WT and P637Q fragments in 5, 10, 25, 50, 100, and 200 mM concentrations (mean \pm SE [error bars]; n = 3) is similar. PTPN12 Pro4 peptide binding to FLNa domains 1, 3, 4 (WT and P637Q mutant), 5, and 6 in 5, 10, 25, 50, 100, and 200 mM concentrations (mean \pm SE [error bars]; n = 3). FLNa4 WT and the P637Q mutant display similar results to both GPIba and Pro4 peptides, suggesting that the peptide binding sites are not affected by the mutation. FLNa domains 3, 5, and 6 display weaker binding toward the PTPN12 Pro4 peptide, while FLNa1 binding to the peptide is unsubstantial.

Discussion

Here, we report the first comprehensive structural and functional characterization of valvulopathy causing mutant protein by combining state-of-the-art structural biology and biophysics methods.

In FLNA-MVD, Force Transmission Is Changed through FLNa

Structural characterization of FLNa3-5 P637Q combining X-ray crystallography, SAXS and MD simulations revealed that, although the mutation does not alter the overall protein fold, local interactions are modified in FLNA-MVD compared with WT FLNa. Accordingly, rather small FLNa structural changes cause the FLNA-MVD phenotype associated with important mitral valve structure abnormalities affecting its function. The crucial question thus addressed the functional consequences of these structural changes. Mechanotransduction of endocardial endothelial cells is known to play a critical role in all aspects of heart development, including chamber morphogenesis and valve development (McCormick and Tzima, 2016), and defects in mechanosensing are known to cause various medical conditions that include cardiac diseases (Herum et al., 2017; Krüger and Linke, 2009; Lyon et al., 2015). FLNa is strongly expressed in endocardial cells during cardiac morphogenesis (Norris et al., 2010) and is, in turn, an important cellular mechanosensing element (Ehrlicher et al., 2011). Therefore, the possibility of altered force transmission ability being linked to the pathogenesis of FLNA-MVD was an appealing hypothesis and was investigated. SMD simulations were applied to the solved atomic detailed structure of FLNa3-5 P637Q to determine whether (1) rod 1 is also force sensitive, and (2) how P637Q mutation influences the force-sensing ability of FLNa. SMD simulations are the only method from which atomic detailed information about forceinduced structural changes can be obtained. Our results clearly show that the FLNa4-5 fragment is force sensitive and that the P637Q mutation changes FLNa's force resilience compared with WT. Based on dynamical network analysis performed for trajectories obtained from SMD simulations, the force propagation pathways are different in WT and P637Q mutated FLNa. In the mutated FLNa, force propagates close to the mutation site, which is not the case with WT. These structural and force propagation path changes have significant impact on the force transmission ability of the mutated FLNa P637Q. Lower forces are also needed to break the FLNa4-FLNa5 interaction in mutant FLNa than in WT FLNa. Accordingly, our results reveal that in FLNa P637Q FLNa response to mechanical stimuli; i.e., mechanosensing. Consequently, FLNa's altered ability to transmit shear forces from the extracellular matrix to the cytoskeleton could be linked to the FLNA-MVD. Recently, the changes in the force transmission ability of FLNa in skeletal dysplasia have been reported (Seppälä et al., 2017). However, it should be noted that, to date, no in vitro or in vivo data have been reported about force-induced FLNa4-5 domain-domain interface openings and how the P637Q mutation influences this. SMD simulation is, however, a well validated method and SMD simulations have correctly predicted the mechanical properties of multiple proteins, such as ankyrin, C-cadherin (Sotomayor, 2015), cellusomes (Verdorfer et al., 2017), and FLNa (Pentikäinen and Ylänne, 2009; Rognoni et al., 2012), as determined by independent atomic force microscopy (Sotomayor, 2015; Verdorfer et al., 2017) or single-molecule experiments (Rognoni et al., 2012). Accordingly, it is reasonable to expect that the performed SMD simulations provide insights and information about force resilience of FLNa.

The FLNa's Interactions Are Affected in FLNA-MVD

FLNa is a scaffold protein that interacts with more than 90 different proteins, including signaling proteins and transmembrane receptors. Changes in these interactions due to diseasecausing mutation, and the following downstream effects, have often been proposed as the reason behind various diseases. GPIba is known to bind between the C and D strands of FLNc4 (Figure 1B; Sethi et al., 2014), the domain where the FLNAMVD P637Q mutation is located. Our results from in vitro binding assays show that the mutation had no effect on GPIba binding on FLNa4. This is in accordance with the FLNa3-5 P637Q structure, which reveals that the GPIba binding site between C and D b strands is not affected by the mutation. PTPN12 and Vimentin have been reported to bind domains 1-8 with a currently unknown binding mechanism (Duval et al., 2015; Kim et al., 2010b, 2010a). Our results using isolated FLNa domains and PTPN12 Pro4 binding domain showed that, although they interact with low binding affinities (in the order of 10th of micromolar; Figure 6), the FLNa domain 4 stands as the main binding domain of PTPN12. The P637Q mutation does not influence PTPN12 Pro4 domain binding to FLNa4 domain. Interestingly, longer FLNa and PTPN12 fragments interact with significantly higher affinities (Kd z 300 nM), and, more interestingly, the P637Q mutation blocks PTPN12 binding to FLNa4-6. The higher affinities observed for longer PTPN12 and FLNa fragments compared with single domains might be due to multiple FLNa binding sites at PTPN12. The opposite effects of the P637Q mutation on Pro4 domain and longer PTPN12 Cterminal fragment binding might originate from differences in the shapes and electrostatic potentials of the main PTPN12 binding domain 4 in WT and P637Q mutant. Pro4 itself is only a 13-amino-acid-long peptide having three consecutive proline residues and two other proline residues. Accordingly, the Pro4 itself is not able to form an a helix or any other stable secondary or tertiary structure but is a flexible peptide and can easily accommodate different binding modes. Although it is within an 18 kDa C-terminal PTPN12 fragment, the Pro4 binding domain is situated in the middle of C-terminal PTPN12 fragment, which restricts the flexibility of the Pro4 binding domain. Therefore, longer PTPN12 fragments are more sensitive to the shape and electrostatic potential of the binding partner. Accordingly, although P637Q mutation causes only small structural changes, these are sufficient to block PTPN12 binding.

Conclusions

Cardiac valve diseases affect ~3% of the population and are the most common cause of cardiac surgery because no drugbased treatment is available. Surgical operations always have a risk and all hospital procedures are expensive. Accordingly, there is a great demand to develop drug therapies to reverse or halt disease progression. This development requires a clear understanding of the underlying molecular mechanisms behind the disease, combined with the structural-level information about the proteins involved. Here, we have investigated the molecular factors that contribute to the pathogenesis of FLNA-MVD caused by FLNa P637Q mutation. Although the completely fine molecular mechanisms linking FLNa P637Q mutation to mitral valve dystrophy remain to be unveiled, our discovery that the mutation increases the sensitivity of a specific binding domain to deformation by mechanical forces is consistent with the unique and heavy cyclic mechanical loads the cardiac valves endure from developmental stages throughout the lifespan and the fact that patients do not exhibit pathologies other than FLNA-MVD (Le Tourneau et al., 2017, 2018). As inherited FLNA-MVD is caused by the missense mutation in FLNa, expressed during cardiac morphogenesis during embryo development, the mutated

protein itself cannot be repaired. A tempting possibility would be to design a small molecule that stabilizes the domain-domain interface at the FLNa4-5 fragment against mechanical force as a possible option for the drug-based treatment.

In addition to changes in FLNa's ability to transmit the force, P637Q mutation hampers FLNa's interactions with PTNP12 C-terminal fragment. PTPN12 is a ubiquitously expressed phosphatase involved in immune response and vascular development. PTPN12 and FLNa participate in the same signaling pathways, such as the small GTPase signaling pathway, and both FLNa and PTPN12 play important roles in cell migration. Therefore, it has earlier been speculated that the FLNa-PTPN12 interaction is important in proper valvular development, and the defects in the interaction may cause the FLNA-MVD (Duval et al., 2015). Based on the results presented here, the defects in FLNa-PTPN12 interactions might indeed have role in the development of FLNA-MVD.

Taken together, our results provide a crucial step toward understanding the underlying molecular mechanism behind valvular dystrophy and a possible objective for the development of drug-based therapeutics.

ACKNOWLEDGMENTS

This work was supported by the Academy of Finland (283481 to U.P.) and the National Science Foundation (NSF) (MCB-1616590 to R.C.B.), the Federation Francaise de Cardiologie (2011, Paris, France), and Inserm Translational Research Grant (2012–2016, Paris, France). The computational work was supported by NIH (9P41GM104601); Blue Waters, the Petascale Computational Resource (PRAC) grant "The Computational Microscope", which is supported by the National Science Foundation (ACI-1713784); Blue Waters sustainedpetascale computing project supported by the National Science Foundation (OCI-0725070 and ACI-1238993), the state of Illinois, and by CSC-Finnish IT Center for Science (2000268 and jyy2516 to U.P.). ESRF is thanked for providing the beamline ID30-A and BM29 access. We are grateful to Arja Mansikkaviita for technical assistance in protein expression and purification. We also thank Lukas Milles and Marcelo Melo for helpful discussions. We thank Mike Maillasson 1-Plateforme IMPACT Biogenouest SFR Franc, ois Bonamy Universite de Nantes for his technical expertise in SPR experiments. Dr. R Capoulade is supported by a grant from Institut de France Fondation Lefoulon-Delalande (Paris, France) and a "Connect Talent" research chair from Region Pays de la Loire and Nantes Metropole (France).

AUTHOR CONTRIBUTIONS

T.J.K.H. cloned, expressed and purified the constructs. T.J.K.H. solved the crystal structure and performed pull-down binding assays. S.L., R.C., and J.M. performed the SPR experiments. T.J.K.H. and U.P. performed the SAXS experiments. T.J.K.H. performed binding assays. U.P. and R.C.B. performed and analyzed SMD simulation data. All authors designed experiments and contributed to the manuscript writing.

DECLARATION OF INTERESTS

The authors declare no competing interests.

REFERENCES

- Adams, P.D., Afonine, P.V., Bunkóczi, G., Chen, V.B., Davis, I.W., Echols, N., Headd, J.J., Hung, L.-W., Kapral, G.J., Grosse-Kunstleve, R.W., et al. (2010). PHENIX: a comprehensive Python-based system for macromolecular structure solution. Acta Crystallogr. Sect. D Biol. Crystallogr. 66, 213–221.
- 2. Baldassarre, M., Razinia, Z., Burande, C.F., Lamsoul, I., Lutz, P.G., and Calderwood, D. (2009). Filamins regulate cell spreading and initiation of cell migration. PLoS One 4, e7830.
- 3. Bernstein, J.A., Bernstein, D., Hehr, U., and Hudgins, L. (2011). Familial cardiac valvulopathy due to filamin A mutation. Am. J. Med. Genet. A 155, 2236–2241.
- 4. Butcher, J.T., and Nerem, R.M. (2007). Valvular endothelial cells and the mechanoregulation of valvular pathology. Philos. Trans. R. Soc. Lond. B Biol. Sci. 362, 1445–1457.
- 5. Chen, V.B., Arendall, W.B., Headd, J.J., Keedy, D.A., Immormino, R.M., Kapral, G.J., Murray, L.W., Richardson, J.S., and Richardson, D.C. (2010). MolProbity: all-atom structure validation for macromolecular crystallography. Acta Crystallogr. Sect. D Biol. Crystallogr. 66, 12–21.
- 6. Darden, T., York, D., and Pedersen, L. (1993). Particle mesh Ewald: an N,log(N) method for Ewald sums in large systems. J. Chem. Phys. 98, 10089–10092.
- 7. Duval, D., Labbé, P., Bureau, L., Le Tourneau, T., Norris, R.A., Markwald, R.R., Levine, R., Schott, J.-J., and Mé rot, J. (2015). MVP-associated filamin A mutations affect FlnA-PTPN12 (PTPPEST) interactions. J. Cardiovasc. Dis. 2, 233–247.
- 8. Ehrlicher, A.J., Nakamura, F., Hartwig, J.H., Weitz, D., and Stossel, T.P. (2011). Mechanical strain in actin networks regulates FilGAP and integrin binding to filamin A. Nature 478, 260–263.
- 9. Emsley, P., Lohkamp, B., Scott, W.G., and Cowtan, K. (2010). Features and development of Coot. Acta Crystallogr. D Biol. Crystallogr. 66, 486–501.
- 10. Feng, Y., Chen, M.H., Moskowitz, I.P., Mendonza, A.M., Vidali, L., Nakamura, F., Kwiatkowski, D.J., and Walsh, C.A. (2006). Filamin A (FLNA) is required for cell-cell contact in vascular development and cardiac morphogenesis. Proc. Natl. Acad. Sci. U S A 103, 19836–19841.
- 11. van der Filer, A., and Sonnenberg, A. (2001). Structural and functional aspects of filamins. Biochim. Biophys. Acta 1538, 99–117.
- 12. Franke, D., and Svergun, D.I. (2009). DAMMIF, a program for rapid ab-initio shape determination in small-angle scattering. J. Appl. Crystallogr. 42, 342–346.
- 13. Franke, D., Petoukhov, M.V., Konarev, P.V., Panjkovich, A., Tuukkanen, A., Mertens, H.D.T., Kikhney, A.G., Hajizadeh, N.R., Franklin, J.M., Jeffries, C.M., et al. (2017). ATSAS 2.8: a comprehensive data analysis suite for small-angle scattering from macromolecular solutions. J. Appl. Crystallogr. 50, 1212–1225.
- 14. Gileadi, O., Burgess-Brown, N.A., Colebrook, S.M., Berridge, G., Savitsky, P., Smee, C.E.A., Loppnau, P., Johansson, C., Salah, E., and Pantic, N.H. (2008). High throughput production of recombinant human proteins for crystallography. Methods Mol. Biol. 426, 221–246.
- 15. Herum, K., Lunde, I., McCulloch, A., and Christensen, G. (2017). The softand hard-heartedness of cardiac fibroblasts: mechanotransduction signaling pathways in fibrosis of the heart. J. Clin. Med. 6, 1–31.
- 16. Humphrey, W., Dalke, A., and Schulten, K. (1996). VMD: Visual molecular dynamics. J. Mol. Graph. 14, 33–38.
- 17. Ithychanda, S.S., Hsu, D., Li, H., Yan, L., Liu, D.D., Liu, D., Das, M., Plow, E.F., and Qin, J. (2009). Identification and characterization of multiple similar ligandbinding repeats in filamin: implication on filamin-mediated receptor clustering and cross-talk. J. Biol. Chem. 284, 35113–43521.
- 18. Izrailev, S., Stepaniants, S., Balsera, M., Oono, Y., and Schulten, K. (1997). Molecular dynamics study of unbinding of the avidin-biotin complex. Biophys. J. 72, 1568–1581.

- 19. Jorgensen, W.L., Chandrasekhar, J., Madura, J.D., Impey, R.W., and Klein, M.L. (1983). Comparison of simple potential functions for simulating liquid water. J. Chem. Phys. 79, 926–935.
- 20. Kabsch, W. (2010). Xds. Acta Crystallogr. D Biol. Crystallogr. 66, 125–132.
- 21. Kim, H., Nakamura, F., Lee, W., Shifrin, Y., Arora, P., McCulloch, C.A., Nakamura, K.H., Lee, F., Shifrin, W., Arora, Y., et al. (2010b). Filamin A is required for vimentin-mediated cell adhesion and spreading. Am. J. Physiol. Cell Physiol. 298, 221–236.
- 22. Kim, H., Nakamura, F., Lee, W., Hong, C., Pé rez-Sala, D., and McCulloch, C.A. (2010a). Regulation of cell adhesion to collagen via beta1 integrins is dependent on interactions of filamin A with vimentin and protein kinase C epsilon. Exp. Cell Res. 316, 1829–1844.
- 23. Konarev, P.V., Volkov, V.V., Sokolova, A.V., Koch, M.H.J., and Svergun, D.I. (2003). PRIMUS: a Windows PC-based system for small-angle scattering data analysis. J. Appl. Crystallogr. 36, 1277–1282.
- 24. Kozin, M., and Svergun, D. (2001). Automated matching of high-and low-resolution structural models. J. Appl. Crystallogr. 34, 33–41.
- 25. Krüger, M., and Linke, W.A. (2009). Titin-based mechanical signalling in normal and failing myocardium. J. Mol. Cell. Cardiol. 46, 490–498.
- 26. Kyndt, F., Gueffet, J.P., Probst, V., Jaafar, P., Legendre, A., Le Bouffant, F., Toquet, C., Roy, E., McGregor, L., Lynch, S.A., et al. (2007). Mutations in the gene encoding filamin A as a cause for familial cardiac valvular dystrophy. Circulation 115, 40–49.
- 27. Lange, O.F., and Grubmüller, H. (2006). Generalized correlation for biomolecular dynamics. Proteins 62, 1053–1061.
- 28. Lehtonen, J.V., Still, D.J., Rantanen, V.V., Ekholm, J., Bjo rklund, D., Iftikhar, Z., Huhtala, M., Repo, S., Jussila, A., Jaakkola, J., et al. (2004). BODIL: a molecular modeling environment for structure-function analysis and drug design. J. Comput. Aided Mol. Des. 18, 401–419.
- 29. Levine, R.A., Hagé ge, A.A., Judge, D.P., Padala, M., Dal-Bianco, J.P., Aikawa, E., Beaudoin, J., Bischoff, J., Bouatia-Naji, N., Bruneval, P., et al. (2015). Mitral valve disease—morphology and mechanisms. Nat. Rev. Cardiol. 12, 689–710.
- 30. Lyon, R.C., Zanella, F., Omens, J.H., and Sheikh, F. (2015). Mechanotransduction in cardiac hypertrophy and failure. Circ. Res. 116, 1462–1476.
- 31. Mackerell, A.D., Jr., Bashford, D., Bellott, M., Dunbrack, R.L., Evanseck, J.D., Field, M.J., Fischer, S., Gao, J., Guo, H., Ha, S., et al. (1998). All-atom empirical potential for molecular modeling and dynamics studies of proteins. J. Phys. Chem. B 102, 3586–3616.
- 32. McCormick, M.E., and Tzima, E. (2016). Pulling on my heartstrings: mechanotransduction in cardiac development and function. Curr. Opin. Hematol. 23, 235–242.
- 33. McCoy, A.J., Grosse-Kunstleve, R.W., Adams, P.D., Winn, M.D., Storoni, L.C., and Read, R.J. (2007). Phaser crystallographic software. J. Appl. Crystallogr. 40, 658–674.
- 34. Nakamura, F., Osborn, T.M., Hartemink, C.A., Hartwig, J.H., and Stossel, T.P. (2007). Structural basis of filamin A functions. J. Cell Biol. 179, 1011–1025.
- 35. Norris, R.A., Moreno-Rodriguez, R., Wessels, A., Merot, J., Bruneval, P., Chester, A.H., Yacoub, M.H., Hage` ge, A., Slaugenhaupt, S.A., Aikawa, E., et al. (2010). Expression of the familial cardiac valvular dystrophy gene, filamin-A, during heart morphogenesis. Dev. Dyn. 239, 2118–2127.
- 36. Panjkovich, A., and Svergun, D.I. (2016). Deciphering conformational transitions of proteins by small angle X-ray scattering and normal mode analysis. Phys. Chem. Chem. Phys. 18, 5707–5719.
- 37. Pentikäinen, U., and Ylänne, J. (2009). The regulation mechanism for the auto-inhibition of binding of human filamin A to integrin. J. Mol. Biol. 393, 644–657.
- 38. Petoukhov, M.V., Konarev, P.V., Kikhney, A.G., and Svergun, D.I. (2007). ATSAS 2.1-Towards automated and web-supported small-angle scattering data analysis. J. Appl. Crystallogr. 40, 223–228.

- 39. Phillips, J.C., Braun, R., Wang, W., Gumbart, J., Tajkhorshid, E., Villa, E., Chipot, C., Skeel, R.D., Kale, L., and Schulten, K. (2005). Scalable molecular dynamics with NAMD. J. Comput. Chem. 26, 1781–1802.
- 40. Playford, M.P., Lyons, P.D., Sastry, S.K., and Schaller, M.D. (2006). Identification of a filamin docking site on PTP-PEST. J. Biol. Chem. 281, 34104–34112.
- 41. Razinia, Z., Mäkelä, T., Ylänne, J., and Calderwood, D. (2012). Filamins in mechanosensing and signaling. Annu. Rev. Biophys. 41, 227–246.
- 42. Rognoni, L., Stigler, J., Pelz, B., Ylänne, J., and Rief, M. (2012). Dynamic force sensing of filamin revealed in single-molecule experiments. Proc. Natl. Acad. Sci. U S A 109, 19679–19684.
- 43. Ruskamo, S., Gilbert, R., Hofmann, G., Jiang, P., Campbell, I.D., Ylänne, J., and Pentikäinen, U. (2012). The Cterminal rod 2 fragment of filamin A forms a compact structure that can be extended. Biochem. J. 446, 261–269.
- 44. Schoeler, C., Bernardi, R.D.C., Malinowska, K.H., Durner, E., Ott, W., Bayer, E., Schulten, K., Nash, M.A., and Gaub, H.E. (2015). Mapping mechanical force propagation through biomolecular complexes. Nano Lett. 15, 7370–7376.
- 45. Seppälä, J., Bernardi, R.C., Haataja, T.J.K., Hellman, M., Pentikäinen, O.T., Schulten, K., Permi, P., Ylänne, J., and Pentikäinen, U. (2017). Skeletal dysplasia mutations effect on human filamins' structure and mechanosensing. Sci. Rep. 7, 4218.
- 46. Sethi, R., and Ylänne, J. (2014). Small-angle x-ray scattering reveals compact domain-domain interactions in the N-Terminal region of filamin C. PLoS One 9, e107457.
- 47. Sethi, A., Eargle, J., Black, A.A., and Luthey-Schulten, Z. (2009). Dynamical networks in tRNA:protein complexes. Proc. Natl. Acad. Sci. U S A 106, 6620–6625.
- 48. Sethi, R., Seppälä, J., Tossavainen, H., Ylilauri, M., Ruskamo, S., Pentikäinen, O.T., Pentikäinen, U., Permi, P., and Ylänne, J. (2014). A novel structural unit in the N-terminal region of filamins. J. Biol. Chem. 289, 8588–8598.
- 49. Sotomayor, M. (2015). Computational exploration of single-protein mechanics by steered molecular dynamics. AIP Conf. Proc. 1703, 030001.
- 50. Stossel, T.P., Condeelis, J., Cooley, L., Hartwig, J.H., Noegel, A., Schleicher, M., and Shapiro, S.S. (2001). Filamins as integrators of cell mechanics and signalling. Nat. Rev. Mol. Cell Biol. 2, 138–145.
- 51. Svergun, D., Barberato, C., and Koch, M.H. (1995). CRYSOL a program to evaluate X-ray solution scattering of biological macromolecules from atomic coordinates. J. Appl. Crystallogr. 28, 768–773.
- 52. Le Tourneau, T., Le Scouarnec, S., Cueff, C., Bernstein, D., Aalberts, J.J.J., Lecointe, S., Mé rot, J., Bernstein, J.A., Oomen, T., Dina, C., et al. (2017). New insights into mitral valve dystrophy: a Filamin-A genotype—phenotype and outcome study. Eur. Heart J. 39, 1269–1277.
- 53. Le Tourneau, T., Mé rot, J., Rimbert, A., Le Scouarnec, S., Probst, V., Le Marec, H., Levine, R.A., and Schott, J.-J. (2018). Genetics of syndromic and non-syndromic mitral valve prolapse. Heart 104, 978–984.
- 54. Tria, G., Mertens, H.D.T., Kachala, M., and Svergun, D.I. (2015). Advanced ensemble modelling of flexible macromolecules using X-ray solution scattering. IUCrJ 2, 207–217.
- 55. Verdorfer, T., Bernardi, R., Meinhold, A., Ott, W., Luthey-Schulten, Z., Nash, M.A., and Gaub, H.E. (2017). Combining in vitro and in silico single molecule force spectroscopy to characterize and tune cellulosomal scaffoldin mechanics. J. Am. Chem. Soc. 139, 17841–17852.
- 56. Volkov, V.V., and Svergun, D.I. (2003). Uniqueness of ab initio shape determination in small-angle scattering. J. Appl. Crystallogr. 36, 860–864.
- 57. Zhou, A.-X., Hartwig, J.H., and Akyürek, L.M. (2010). Filamins in cell signaling, transcription and organ development. Trends Cell Biol. 20, 113–123.

CONTACT FOR REAGENT AND RESOURCE SHARING

Further information and request for reagents may be directed to, and will be fulfilled by the Lead Author Dr. Ulla Pentikäinen (ulla.pentikainen@utu.fi).

METHODS

Recombinant Proteins

FLNa domains were cloned to pGTvL1-SGC vector (Structural Genomics Consortium, University of Oxford) using the ligase independent method (Gileadi et al., 2008) and the PTN12 fragment (aa 600-780) cloned into the pET23b plasmid. The P637Q and PTPN12 mutations were introduced to the desired expression constructs using the QuikChange II Site-Directed Mutagenesis Kit (Agilent Technologies). All the expression plasmids were verified by sequencing. The production of Glutathione S-transferase (GST) fusion proteins occurred at 30oC for 4-6 h using Escherichia coli BL21 Gold cells. Complete lysis of the cells was achieved using the EmulsiFlex-C3 homogenizer (Avestin) and lysates were cleared by centrifugation at 35 000 x g for 30 min at 4oC. The GST-fusion proteins were captured using Protino Glutahione Agarose 4B (Macherey-Nagel) and the GST was cleaved at 4oC for 16h by Tobacco Etch Virus (TEV) protease (Invitrogen, Life Technologies). HiLoad 26/60 Superdex 75 column (GE Healthcare) was utilized in the size exclusion chromatography of the desired fragments in 20 mM Tris pH 8.0, 100 mM NaCl, 1 mM DTT using an A" KTA prime system (GE Healthcare). Amicon Ultra centrifugal devices (Merck Millipore) were used for concentrating the proteins for downstream experiments. The verification of homodispersity of each protein was done by analytical gel filtration and SDS-PAGE. 6-His tagged PTPN12 fragments were also produced in BL21 and purified on nickel beads (Macherey Nagel) using imidazole 250mM elution. Purified proteins were dialyzed against phosphate buffer solution and quantified and analysed by PAGE before using in SPR experiments.

Protein Crystallography

The initial FLNa3-5 P637Q crystals were obtained from vapour diffusion trials mixing equal volumes of 1.0 mM protein and reservoir solution resulting in 400 nl hanging drops at room temperature. Stable crystals were obtained in 0.05 M ammonium citrate, 18 % PEG3350. The crystals were flash frozen in reservoir solution supplemented with 20 % ethylene glycol and the diffraction data were collected at beamline ID30A-3 (wavelength 0.961 Å) at 100 K at the European Synchrotron Radiation Facility (ESRF), Grenoble, France. The data were processed using XDS (Kabsch, 2010) and the structure was solved using Phaser (McCoy et al., 2007). FLNa3-5 (PBD ID: 4M9P) (Sethi et al., 2014) was used as the model in the rotation and translation search. The structure was built using Coot (Emsley et al., 2010), refined with Phenix (Adams et al., 2010) and validated using MolProbity (Chen et al., 2010). The Ramachandran plot illustrates 95 % of residues in the favoured region with zero outliers. The final processing and refinement statistics are summarized in Table 1. The structure factors and atomic coordinates were deposited in the PDB with ID 6EW1. PyMOL Molecular Graphics System, version 0.99, Schroʻ dinger, LCC was used for preparing all the crystallographic images. Root mean square deviation between the FLNa3-5 WT and FLNa3-5 P637Q mutant structures was calculated using Bodil (Lehtonen et al., 2004).

SAXS

BM29 beamline, ESRF, Grenoble, France was used for collecting the SAXS data on a PILATUS 1M image plate using sample to detector distance of 2.9 m and a wavelength of 1.0 Å (momentum transfer range 0.01 < q < 5 nm-1). Three different protein concentrations (1.0, 2.0 and 4.0 mg/ml) were used in the data acquisition. DTT was added freshly to 10 mM in the gel filtration buffer prior to measurements. ATSAS software package was utilized in the data processing (Franke et al., 2017). PRIMUS (Konarev et al., 2003) was used for data reduction and DATGNOM (Petoukhov et al., 2007) for the calculation of distance distribution functions. The Porod volumes were estimated using DATPOROD program in ATSAS (Franke et al., 2017). Guinier analysis performed using PRIMUS (Konarev et al., 2003), and distance distribution functions calculated using DATGNOM (Petoukhov et al., 2007) provided the estimates for radius of gyration (Rg) and maximum dimensions (Dmax) of the particles. Apparent particle aggregation or repulsion was excluded in the Guinier analysis. SREFLEX (Panjkovich and Svergun, 2016) was used for estimating the flexibility of the crystal structures to improve the fit in CRYSOL (Svergun et al., 1995) that was used for evaluating the scattering from the high resolution structures and fitting them to experimental data. DAMMIF (Franke and Svergun, 2009) was used for generating in total twenty ab initio shape envelopes that were subsequently aligned against the most probable, then averaged and ultimately filtered in the DAMAVER program suite (Volkov and Svergun, 2003). The obtained models were refined and fitted against the scattering data using DAMMIN (Franke and Svergun, 2009). The flexibility of the selected FLNa fragments were examined using the ensemble optimization method (EOM, version 2.0) (Tria et al., 2015) that results in comparable Rg and Dmax distribution profiles. In EOM calculations, FLNa3, FLNa4, and FLNa5 were used rigid bodies. The final overlaying of the crystal structures and the ab initio models was done in SUPCOMB (Kozin and Svergun, 2001). The SAXS data were deposited to Small Angle Scattering Biological Data Bank (SASBDB). See Table 2 for the summary of the SAXS data analysis. PyMOL Molecular Graphics System, version 0.99, Schroedinger, LCC was used for preparing all the SAXS images.

Binding Assays

The binding assays were performed using the PTPN12 Pro4-peptide (672DSPPPLPERTPES684, UNIPROT ID Q05209.3) synthetized by ProteoGenix and the GPIba-peptide (599LRGSLPTFRSSLFLWVRPNGRV622, UNIPROT ID P07359) synthetized by GenScript. The peptides were coupled to NHS-activated Sepharose TM 4 Fast Flow (GE Healthcare) following manufacturer's instructions. FLN protein fragments were prepared in assay buffer, 20 mM Tris; pH 7.4, 150 mM NaCl, 1 % Triton X-100 for each concentration series (0, 5, 10, 25, 50, 100 and 200 mM). The binding occurred at room temperature for 1 h by mixing the samples with 50 ml of the Sepharose. The resin was then washed with 2 x 15 bed volumes of assay buffer using a centrifuge at 2000 x g for 2 min. Finally, 10 ml of 2X SDSelectrophoresis sample buffer was used for eluting the proteins that were subsequently separated on 12 % gels according to their molecular mass using SDS-PAGE. The gels were stained with Coomassie Brilliant Blue R-250 and imaged digitally. The intensities of each sample were assessed using ImageJ. GraphPad Prism 5 (GraphPad Software) was used for plotting the data with standard error of the mean of each fragment. The FLN binding to the peptides was normalized against the FLN loading controls in each experiment. The binding assays were repeated 2-4 times for each fragment.

Surface Plasmon Resonance Experiment

All SPR experiments were conducted on the Biacore 3000 system. The experiments were carried out at 25oC, using HBSEP as running buffer, 0.15 M NaCl, 0.01 M HEPES, 3 mM EDTA, 0.005% v/v P20 (pH 7.4). Purified PTPN12 fragments were immobilized on CM5 sensor chips (GE Healthcare) by amine coupling as recommended by supplier for about 200-300 resonance units (RU). Samples of purified FLNa4-6 WT and P637Q mutants were diluted in the running buffer and injected in Single Cycle Kinetics (SCK) mode at 5 different concentrations (0.31, 0.62, 1.25, 2.50, 5.00 mM) at a flow rate of 30 ml/min over the chip surface. Binding surfaces were regenerated to remove bound analyte by injecting 50mM NaOH during 30s. This regeneration condition removed analyte completely but retained the surface binding capacity of the PTPN12 functionalized chip. Kinetic constants were calculated by global fitting of the data to a 1:1 Langmuir binding model (SCK) after subtracting the control surface, using the BIAevaluation software, version 4.0.1.

MD Simulations

The atomic coordinates for FLNa4-5 WT were taken from the crystal-structure of FLNa3-5 (PBD ID: 4M9P) (Sethi et al., 2014), whereas those for FLNa4-5 P637Q were taken from the X-ray structure solved here (PBD ID: 6EW1). Systems were solvated and the net charge of the protein was neutralized using sodium atoms as counter-ions, which were randomly arranged in the solvent. The CHARMM36 force field (Mackerell et al., 1998) along with the TIP3 water model (Jorgensen et al., 1983) was used to describe all systems. Before SMD simulations, the systems were first submitted to an energy minimization protocol for 1,000 steps and equilibrated using standard MD simulations. The MD simulations were performed employing the NAMD molecular dynamics package (Phillips et al., 2005) assuming periodic boundary conditions in the NpT ensemble with temperature maintained at 300 K using Langevin dynamics for temperature coupling and kept at 1 bar. A distance cut-off of 11.0 Å was applied to short range, nonbonded interactions, whereas long-range electrostatic interactions were treated using the particle-mesh Ewald (PME) method (Darden et al., 1993). The equations of motion were integrated using multiple time step scheme to update the van der Waals interactions every two steps and electrostatic interactions every four steps. The time step of integration was chosen to be 2 fs for all simulations performed. The systems were equilibrated so that first Ca-atoms of backbone were harmonically restrained for 1 ns followed by 1 ns keeping the whole system freely. The MD simulation were then run for 100 ns and repeated for three times. The obtained trajectories were then analysed using VMD (Humphrey et al., 1996).

SMD Simulations

The systems were built and equilibrated as described above for MD simulations, only the TIP3P water box was designed larger to ensure the full solvation also the stretched FLNa fragments. SMD simulations (Izrailev et al., 1997) were performed using constant velocity stretching (SMD-CV protocol) employing pulling speeds: 2.5 Å /ns. In all simulations, SMD was employed by restraining the position of N-terminus of domain 16 harmonically and the Ca-atom of the most C-terminal residue was assigned as SMDatom. The force applied to the harmonic spring is then monitored during the time of the molecular dynamics simulation. The pulling point was moved with constant velocity along the z-axis and due to the

single anchoring point and the single pulling point the system is quickly aligned along the z-axis. SMD simulations were repeated in an enhanced sampling approach (Schoeler et al., 2015) for 50 times for WT FLNa4-5 fragment and 30 times for P637Q FLNa4-5 fragment, and comparable results were obtained. All analyses of MD trajectories were carried out employing VMD and its plugins (Humphrey et al., 1996). Force propagation networks were analysed using same protocol described in (Verdorfer et al., 2017). The communities formed in the systems were calculated by employing dynamic network analysis (Sethi et al., 2009) and generalized correlation (Lange and Grubmüller, 2006).

QUANTIFICATION AND STATISTICAL ANALYSIS

X-ray Crystallography

Statistics generated from X-ray crystallography data processing, refinement, and structure validation are displayed in Table 1.

SAXS

SAXS data validation is shown in Table 2.

Binding Assays

Binding assays were performed in triplicates (n=3) and results are expressed as mean +/SE. Analyses were done with GraphPad Prism software (GraphPad).

DATA AND SOFTWARE AVAILABILITY

The accession number for the FLNa structure reported in this paper PDB: 6EW1.